


# Effective time step analysis for the Allen–Cahn equation with a high-order polynomial free energy

Seunggyu Lee<sup>1,2</sup> | Sungha Yoon<sup>3</sup> | Chaeyoung Lee<sup>4</sup> | Sangkwon Kim<sup>4</sup> |  
Hyundong Kim<sup>5</sup> | Junxiang Yang<sup>6</sup> | Soobin Kwak<sup>4</sup> | Youngjin Hwang<sup>4</sup> |  
Junseok Kim<sup>4</sup> 

<sup>1</sup>Division of Applied Mathematical Sciences, Korea University, Sejong, Republic of Korea

<sup>2</sup>Biomedical Mathematics Group, Pioneer Research Center for Mathematical and Computational Sciences, Institute for Basic Science, Daejeon, Republic of Korea

<sup>3</sup>Institute of Mathematical Sciences, Ewha Womans University, Seoul, Republic of Korea

<sup>4</sup>Department of Mathematics, Korea University, Seoul, Republic of Korea

<sup>5</sup>Institute for the Advanced Study of Human Biology (WPI-ASHBi), Kyoto University Institute for Advanced Study, Kyoto University, Kyoto, Japan

<sup>6</sup>School of Computer Science and Engineering, Sun Yat-Sen University, Guangzhou, China

## Correspondence

Junseok Kim, Department of Mathematics, Korea University, Seoul 02841, Republic of Korea.  
Email: [cfdkim@korea.ac.kr](mailto:cfdkim@korea.ac.kr)

## Funding information

Ministry of Education, Grant/Award Number: NRF-2020R1A6A3A13077105; Ministry of Science and ICT, South Korea, Grant/Award Number: 2019R1A6A1A11051177; Ministry of Science, ICT and Future Planning, Grant/Award Number: 2020R1A2C1A01100114

## Abstract

An effective time step analysis to the linear convex splitting scheme for the Allen–Cahn equation with a high-order polynomial free energy is presented in this article. Although the convex splitting scheme is unconditionally stable, using a large time step causes a time step rescaling effect, leading to delayed dynamics of the governing equation. We verify this problem by comparing it with a reformulated semi-implicit scheme using the effective time step. Theoretical results show that the discrete energy stability and maximum-principle hold, and the numerical results demonstrate that the time step rescaling issue can be resolved using the effective time step. We confirm that slow dynamics due to high-order potential is alleviated by the time step modification through the results of motion by mean curvature.

## KEYWORDS

Allen–Cahn equation, effective time step, high-order polynomial free energy, linear convex splitting

## 1 | INTRODUCTION

In this article, an effective time step analysis for the Allen–Cahn (AC) equation with a high-order polynomial free energy potential is presented. We denote this equation as the high-order Allen–Cahn (hAC) equation hereafter. The classical AC equation is as follows:<sup>1</sup>

$$\frac{\partial \phi(\mathbf{x}, t)}{\partial t} = -\frac{F'(\phi(\mathbf{x}, t))}{\epsilon^2} + \Delta \phi(\mathbf{x}, t), \quad \mathbf{x} \in \Omega, \quad t > 0, \quad (1)$$

where  $\phi(\mathbf{x}, t)$  is the difference between the two concentrations in a domain  $\Omega \subset \mathbb{R}^d$ , for  $d = 2, 3$ , with the zero Neumann boundary condition, that is,  $\partial \phi / \partial \mathbf{n} = 0$  on  $\partial \Omega$  where  $\partial / \partial \mathbf{n}$  is the normal derivative. The free energy function is

$F(\phi) = 0.25(\phi^2 - 1)^2$ , and  $\epsilon$  is a positive parameter related to the interfacial thickness. We note that Equation (1) can be derived as the  $L^2$ -gradient flow of the following total energy functional:

$$\mathcal{E}(\phi) = \int_{\Omega} \left( \frac{F(\phi)}{\epsilon^2} + \frac{1}{2} |\nabla \phi|^2 \right) dx. \quad (2)$$

Differentiating Equation (2) with respect to time yields the non-increasing energy over time as follows:

$$\begin{aligned} \frac{d\mathcal{E}(\phi)}{dt} &= \int_{\Omega} \left( \frac{F'(\phi)}{\epsilon^2} \phi_t + \nabla \phi \cdot \nabla \phi_t \right) dx \\ &= \int_{\Omega} \left( \frac{F'(\phi)}{\epsilon^2} - \Delta \phi \right) \phi_t dx = - \int_{\Omega} \phi_t^2 dx \leq 0. \end{aligned}$$

The classical AC equation and modified forms have been widely employed for phase transition,<sup>1,2</sup> image processing,<sup>3,4</sup> topology optimization,<sup>5,6</sup> multiphase flows,<sup>7-9</sup> mechanical behavior of thin-walled superalloys,<sup>10</sup> dendrite growth,<sup>11,12</sup> motion by mean curvature,<sup>13,14</sup> microscopic fluctuating strain,<sup>15</sup> damage field of sensitivity-uncertainty quantification framework<sup>16</sup> and so forth. As such, many scientific problems have been solved through the numerical application of the AC equation. For the numerical solution to diffuse-interface systems, such as the AC equation, a sufficiently large number of grid points is required to discretize the phase interface layer.<sup>17</sup> As one way to properly compute the diffuse-interface even in relatively coarse grids for computational efficiency, the high-order polynomial free energy function was recently applied.<sup>18,19</sup> In particular, the authors in Reference 19 dealt with the use of the hAC equation especially focusing on the advantages of employing the high-order free energy function in applications. The high-order polynomial free energy function is defined as follows:

$$F_m(\phi) = 0.25(\phi^{2m} - 1)^2, \quad (3)$$

where  $m$  is a positive integer. Please refer to References 18,19 and the references therein for further details. Figure 1 shows the polynomial free energy functions (3), for  $m = 1, 2, 3, 4$ , and  $5$ .

To resolve these scientific problems, several numerical solvers for the AC equation have been developed so far. Since the other intrinsic property of the AC equation is the maximum-principle preserving<sup>20</sup> along with the energy dissipation law above, research on schemes that inherit these properties at the discrete level has been recently presented.<sup>21-24</sup> Feng et al. developed a linear second-order scheme based on the leapfrog scheme with a stabilized term.<sup>21</sup> Under moderate constraints on the time step, the maximum-principle is preserved at a discrete level. In Reference 22, the authors provided a high-order explicit scheme for the AC equation, which is up to the fourth-order in time and is based on the integrating factor Runge–Kutta method. The authors adopted the stabilizing parameter and projection method to ameliorate the restriction on the time step and achieved the first-order and fourth-order for stiff and non-stiff terms, respectively. Wang et al. also provided a linear energy stable and maximum-principle preserving method for the AC equation.<sup>23</sup> The authors discussed a stabilized energy factorization to treat the common double-well potential semi-implicitly. Li and Song developed a reduced-order finite difference scheme which is of second-order in time based on the proper orthogonal

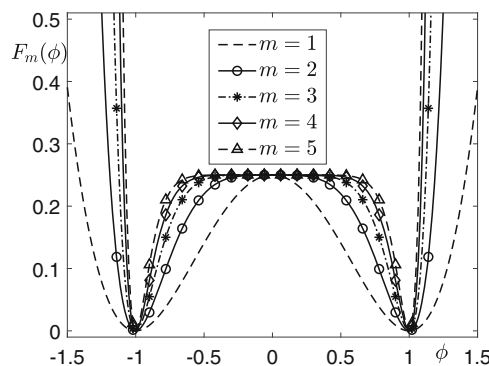


FIGURE 1 High-order polynomial free energy functions.

decomposition technique.<sup>24</sup> The authors confirmed that the computational efficiency of the new framework is much better than that of the conventional framework. Furthermore, the second-order nonlinear interior penalty discontinuous Galerkin method was proposed by Li et al. in Reference 25. In particular, the authors focused on the convergence of the numerical interface via the proposed scheme in a curvature-driven geometric flow. Recently, Montanelli and Bootland proposed an exponential integration formula and compared its performance to stiff partial differential equations, including the AC equation.<sup>26</sup> Research using an adaptive physics-informed neural network on phase-field models including the AC equation was embraced instead of the traditional solver for partial differential equations.<sup>27</sup>

As mentioned above, the maximum-principle preservation is accompanied by an appropriate restriction on the time step. To satisfy the maximum-principle preservation regardless of the order in the hAC equation, we adopt the concept of the linear convex splitting (CS) scheme reported by Eyre as follows:<sup>28</sup>

$$\frac{\phi^{n+1} - \phi^n}{\Delta t} = -\frac{2\phi^{n+1}}{\epsilon^2} - \frac{(\phi^n)^3 - 3\phi^n}{\epsilon^2} + \Delta\phi^{n+1}. \quad (4)$$

Note that the pointwise boundness of Equation (4) was demonstrated in Reference 29. This scheme is deduced from the following factorization of the free energy functional:

$$\begin{aligned} \mathcal{E}(\phi) &= \mathcal{E}^c(\phi) - \mathcal{E}^e(\phi) \\ &= \int_{\Omega} \left( \frac{1}{2} |\nabla\phi|^2 + \frac{1}{\epsilon^2} \phi^2 \right) dx - \int_{\Omega} \left( -\frac{1}{4\epsilon^2} (\phi^2 - 1)^2 + \frac{1}{\epsilon^2} \phi^2 \right) dx, \end{aligned} \quad (5)$$

where the contractive part  $\mathcal{E}^c(\phi)$  and expansive part  $-\mathcal{E}^e(\phi)$  are treated implicitly and explicitly, respectively. Let  $\langle \varphi, \psi \rangle := \int_{\Omega} \varphi\psi dx$  be the  $L^2$ -inner product and  $\|\varphi\| := \sqrt{\langle \varphi, \varphi \rangle}$  be the  $L^2$ -norm. Because Equation (1) is a gradient flow of (2),  $\langle \phi, J_{\mathcal{E}}\phi \rangle \geq \lambda$  for  $\lambda \in \mathbb{R}$  where  $J_{\mathcal{E}}$  is the Jacobian of  $\delta\mathcal{E}/\delta\phi$ . We reformulate Equations (4) and (5) to fit the hAC equation in Section 2.

The main objective of this study is to present the effective time step analysis to the unconditionally gradient stable linear CS method for the hAC equation. The CS scheme is handed down to implement the hAC equation in an arbitrary order; however, studying the effective time step on the slow dynamics that occur as the order increases is necessary.<sup>19</sup> In fact, the CS scheme for the AC equation (4) can be interpreted as a semi-implicit scheme with different time step scaling as follows:

$$\frac{\phi^{n+1} - \phi^n}{\frac{\epsilon^2 \Delta t}{2\Delta t + \epsilon^2}} = -\frac{1}{\epsilon^2} [(\phi^n)^3 - \phi^n] + \Delta\phi^{n+1}. \quad (6)$$

Several prior studies have focused on the relation between CS and the fully implicit scheme.<sup>30-32</sup> According to references and those therein, the CS scheme may lack numerical accuracy unless the time step is sufficiently small. Thus, numerical accuracy can be improved by adopting a fully implicit scheme using a small time step; however, the fully implicit interpretation is difficult to employ owing to the high nonlinearity of the hAC equation. Therefore, we adopt the linear CS scheme (4) and performed the effective time step analysis. We then rewrite Equation (6) to fit right in the hAC equation and investigate the effect of modified time steps in the rewritten equation with respect to order  $m$ .

The remainder of this article is organized as follows. In Section 2, we explain the numerical solution with the effective time step and analyze the two intrinsic properties of the hAC equation at the discrete level. In Section 3, numerical simulations are conducted to support analytical results. In Section 4, conclusions and future work are discussed.

## 2 | NUMERICAL ANALYSIS

We employ the conventional unconditionally energy stable linear CS scheme using the original time step to the hAC equation owing to the high nonlinearity and interpret this scheme as the reformulated semi-implicit scheme using the effective time step in this section. Moreover, the least upper bound of the effective time step is presented. Numerical solution is derived from the rewritten semi-implicit scheme and discrete cosine transform framework. Theoretical results for the energy stability and maximum-principle preservation of the linear CS scheme are also provided. We extend this result to hold even in the reformulated semi-implicit scheme.

## 2.1 | Linear CS scheme

The total energy (2) is modified using the high-order free energy function (3), as follows:

$$\mathcal{E}(\phi) = \int_{\Omega} \left( \frac{F_m(\phi)}{\epsilon^2} + \frac{1}{2} |\nabla \phi|^2 \right) dx. \quad (7)$$

Using the variational approach yields the following  $L^2$ -gradient flow:

$$\frac{\partial \phi}{\partial t} = -\frac{\delta \mathcal{E}}{\delta \phi} = -\frac{m}{\epsilon^2} (\phi^{4m-1} - \phi^{2m-1}) + \Delta \phi. \quad (8)$$

To employ the linear CS scheme based on Reference 28, the energy functional (7) is split into contractive and expansive parts as follows:

$$\begin{aligned} \mathcal{E}(\phi) &= \mathcal{E}^c(\phi) - \mathcal{E}^e(\phi) \\ &= \int_{\Omega} \left( \frac{|\nabla \phi|^2}{2} + \frac{\alpha}{2\epsilon^2} \phi^2 \right) dx - \int_{\Omega} \left( -\frac{(\phi^{2m} - 1)^2}{4\epsilon^2} + \frac{\alpha}{2\epsilon^2} \phi^2 \right) dx, \end{aligned} \quad (9)$$

where  $\alpha$  is a stabilizing constant that allows  $\mathcal{E}^e(\phi)$  to be convex. If  $\mathcal{E}^e(\phi)$  is not convex, then there might be multiple equilibria of Equation (4) for  $\lambda < 0$ ; hence, the convexity of  $\mathcal{E}^e(\phi)$  yields  $\langle \phi, J_{\mathcal{E}^e} \phi \rangle \geq -\lambda$  and then Equation (4) is consistent and unconditionally stable.<sup>33</sup> Note that the contractive part  $\mathcal{E}^c(\phi)$  is convex by construction. Recall that the terms are treated implicit and explicit ways, respectively. Let  $\phi^n$  be an approximation of  $\phi(\mathbf{x}, n\Delta t)$ , where  $\Delta t$  is the discretized time step. The following semi-discretized equation is derived by treating the contractive and expansive terms in Equation (9) as implicit and explicit ways, respectively, and applying to Equation (8):

$$\frac{\phi^{n+1} - \phi^n}{\Delta t} = -\frac{m}{\epsilon^2} (\phi^n)^{4m-1} + \frac{m}{\epsilon^2} (\phi^n)^{2m-1} - \frac{\alpha}{\epsilon^2} (\phi^{n+1} - \phi^n) + \Delta \phi^{n+1}. \quad (10)$$

The second-order Taylor expansion to  $\mathcal{E}(\phi)$  is used to show the non-increasing discrete energy over time for any  $\Delta t > 0$  as follows:

$$\begin{aligned} \mathcal{E}(\phi^{n+1}) - \mathcal{E}(\phi^n) &= [\mathcal{E}^c(\phi^{n+1}) - \mathcal{E}^e(\phi^{n+1})] - [\mathcal{E}^c(\phi^n) - \mathcal{E}^e(\phi^n)] \\ &= [\mathcal{E}^c(\phi^{n+1}) - \mathcal{E}^c(\phi^n)] - [\mathcal{E}^e(\phi^{n+1}) - \mathcal{E}^e(\phi^n)] \\ &\leq \left\langle \frac{\delta}{\delta \phi} (\mathcal{E}^c(\phi^{n+1}) - \mathcal{E}^e(\phi^{n+1})), \phi^{n+1} - \phi^n \right\rangle \\ &= \left\langle -\frac{\phi^{n+1} - \phi^n}{\Delta t}, \phi^{n+1} - \phi^n \right\rangle \\ &= -\frac{1}{\Delta t} \|\phi^{n+1} - \phi^n\|^2 \leq 0, \end{aligned} \quad (11)$$

when both contractive and expansive parts are convex. Therefore,  $\alpha$  is determined so that the expansive term satisfies the convexity as follows:

$$\frac{\delta^2 \mathcal{E}^e(\phi)}{\delta \phi^2} = -\frac{m(4m-1)}{\epsilon^2} \phi^{4m-2} + \frac{m(2m-1)}{\epsilon^2} \phi^{2m-2} + \frac{\alpha}{\epsilon^2} \geq 0. \quad (12)$$

Thus, we conclude that  $\alpha$  can be determined using Equation (12) as follows:

$$\alpha \geq m(4m-1) - m(2m-1) = 2m^2, \quad (13)$$

if the absolute maximum value of  $\phi$  does not exceed 1.

To prove a discrete maximum-principle property, let  $|\phi^n| \leq \|\phi^n\|_{L^\infty} \leq 1$ , where  $\|\varphi\|_{L^\infty} := \sup_{\mathbf{x} \in \Omega} |\varphi(\mathbf{x})|$ , and rewrite Equation (10) as follows:

$$\left(\frac{1}{\Delta t} + \frac{\alpha}{\epsilon^2}\right) \phi^{n+1} - \Delta \phi^{n+1} = \left(\frac{1}{\Delta t} + \frac{\alpha}{\epsilon^2}\right) \phi^n + \frac{m}{\epsilon^2} (\phi^n)^{2m-1} (1 - (\phi^n)^{2m}). \tag{14}$$

Taking the  $L^2$ -inner product with  $\mathbf{1}$ , where  $\mathbf{1}(\mathbf{x}) = 1$  for all  $\mathbf{x} \in \Omega$ , on the left-hand side of Equation (14), we have

$$\begin{aligned} \left(\frac{1}{\Delta t} + \frac{\alpha}{\epsilon^2}\right) \langle \phi^{n+1}, \mathbf{1} \rangle - \langle \Delta \phi^{n+1}, \mathbf{1} \rangle &= \left(\frac{1}{\Delta t} + \frac{\alpha}{\epsilon^2}\right) \langle \phi^{n+1}, \mathbf{1} \rangle + \langle \nabla \phi^{n+1}, \nabla \mathbf{1} \rangle - \int_{\partial \Omega} \nabla \phi^{n+1} \cdot \mathbf{n} d\sigma \\ &= \left(\frac{1}{\Delta t} + \frac{\alpha}{\epsilon^2}\right) \langle \phi^{n+1}, \mathbf{1} \rangle. \end{aligned} \tag{15}$$

By applying the triangle inequality and (15) to Equation (14) yields

$$\left(\frac{1}{\Delta t} + \frac{\alpha}{\epsilon^2}\right) \langle |\phi^{n+1}|, \mathbf{1} \rangle \leq \left(\frac{1}{\Delta t} + \frac{\alpha}{\epsilon^2}\right) \langle |\phi^n|, \mathbf{1} \rangle + \frac{m}{\epsilon^2} \langle \mathbf{1} - |\phi^n|^{2m}, \mathbf{1} \rangle. \tag{16}$$

We now suppose that  $\|\phi^{n+1}\|_{L^\infty} \geq |\phi^{n+1}(\mathbf{x}_0)| > 1$  for some  $\mathbf{x}_0 \in \Omega$ .

Subsequently, we deduce the following from (16):

$$\begin{aligned} \left(\frac{1}{\Delta t} + \frac{\alpha}{\epsilon^2}\right) \langle |\phi^{n+1}| - |\phi^n|, \mathbf{1} \rangle &\leq \frac{m}{\epsilon^2} \langle \mathbf{1} - |\phi^n|, \mathbf{1} + |\phi^n| + \dots + |\phi^n|^{2m-1} \rangle \\ &< \frac{m}{\epsilon^2} \langle |\phi^{n+1}| - |\phi^n|, \mathbf{1} \rangle \sup_{\mathbf{x} \in \Omega} (\mathbf{1} + |\phi^n| + \dots + |\phi^n|^{2m-1}). \end{aligned} \tag{17}$$

By the assumptions  $\|\phi^n\|_{L^\infty} \leq 1$  and  $\|\phi^{n+1}\|_{L^\infty} > 1$ , we get

$$\left(\frac{1}{\Delta t} + \frac{\alpha}{\epsilon^2}\right) < \frac{m}{\epsilon^2} \sum_{i=1}^{2m} 1 = \frac{2m^2}{\epsilon^2}. \tag{18}$$

Rearranging (18) yields

$$\frac{\epsilon^2}{\Delta t} < -\alpha + 2m^2, \tag{19}$$

which is a contradiction when  $\alpha \geq 2m^2$  for all positive integers  $m$ . In other words, the maximum-principle property  $\|\phi^{n+1}\|_{L^\infty} \leq 1$  holds when  $\alpha \geq 2m^2$ . This implies that the convexity condition (13) holds, and we can then fix  $\alpha = 2m^2$ .

In the next step, we prove that scheme (10) is uniquely solvable. Find  $\phi \in H^1(\Omega)$  such that

$$\langle \phi, \phi \rangle - \Delta t \left\langle \frac{\delta}{\delta \phi} (\mathcal{E}^c(\phi) - \mathcal{E}^e(\phi^n)), \phi \right\rangle = \langle \phi^n, \phi \rangle, \tag{20}$$

for any  $\phi \in H^1(\Omega)$ . Consider the following functional:

$$G(\phi) = \langle \phi, \phi \rangle - \Delta t \left\langle \frac{\delta}{\delta \phi} (\mathcal{E}^c(\phi) - \mathcal{E}^e(\phi^n)), \phi \right\rangle - \langle \phi^n, \phi \rangle. \tag{21}$$

Then,  $G(\phi)$  is strictly convex because the three terms in (21) are quadratic, convex, and linear in order, respectively, and  $\delta_\phi G(\phi)$  is equal to Equation (20). This implies that  $\phi^{n+1} \in H^1(\Omega)$  is a unique minimizer of  $G$  if and only if Equation (20) holds for any  $\phi \in H^1(\Omega)$ , that is,

$$\frac{\phi^{n+1} - \phi^n}{\Delta t} = \frac{\delta}{\delta \phi} (\mathcal{E}^c(\phi^{n+1}) - \mathcal{E}^e(\phi^n)), \tag{22}$$

which is equivalent to Equation (10). Therefore, Equation (10) is uniquely solvable.

## 2.2 | Semi-implicit scheme using the effective time step

We can rewrite Equation (10) as follows:

$$\frac{\phi^{n+1} - \phi^n}{\Delta t_e} = -\frac{m}{\epsilon^2}(\phi^n)^{4m-1} + \frac{m}{\epsilon^2}(\phi^n)^{2m-1} + \Delta\phi^{n+1}, \quad (23)$$

which is a semi-implicit scheme that uses the following effective time step:

$$\Delta t_e = \frac{\Delta t}{1 + 2m^2\Delta t/\epsilon^2}. \quad (24)$$

We denote the least upper bound of  $\Delta t_e$  by  $\Delta t_e^\infty := \sup \Delta t_e = \epsilon^2/2m^2$ . Figure 2 shows the upper bound of the effective time step for each order  $m$ . We consider  $\epsilon = 0.005, 0.0075$ , and  $0.01$  in this case. As depicted in Figure 2, the upper bound becomes lower as the order  $m$  increases. In fact, the linear CS scheme is unconditionally stable, but if the time step is large, the numerical solution may differ from the exact solutions. More precisely, a large time step scale causes delayed dynamics in the governing equation. In addition, it can exacerbate slow dynamics resulting from high-order potentials, which is reported in a previous study.<sup>19</sup> Therefore, we evaluate the numerical solution using the effective time step (24) in order to alleviate slow dynamics. Note that the scale of the effective time step is not significantly related to the dimensions of the domain. Furthermore, two intrinsic properties of the hAC equation—the energy stability and maximum-principle preserving—are maintained in the rewritten scheme (23).

We conclude this subsection by verifying that the accuracy of the linear CS scheme is still of first-order when that of the semi-implicit scheme is of first-order. In other words, the first-order accuracy of the linear CS can be guaranteed only for the time step scale that maintains the first-order accuracy in the semi-implicit scheme. For simplicity, we assign the errors of the linear CS and semi-implicit schemes as  $e_{CS}$  and  $e_{SI}$ , respectively, which are defined as follows:

$$e_{CS}^{n+1} = \Delta t \left( -\frac{m}{\epsilon^2} ((\phi^n)^{4m-1} - (\phi^n)^{2m-1}) - \frac{2m^2}{\epsilon^2} (\phi^{n+1} - \phi^n) + \Delta\phi^{n+1} \right), \quad (25)$$

$$e_{SI}^{n+1} = \Delta t \left( -\frac{m}{\epsilon^2} ((\phi^n)^{4m-1} - (\phi^n)^{2m-1}) + \Delta\phi^{n+1} \right). \quad (26)$$

Now, we assume that the semi-implicit scheme is of first order, that is,  $\|e_{SI}^{n+1}\| \leq K\Delta t$  for some  $K > 0$  and  $\Delta t \leq \Delta t_e^\infty$ . Then, by rearranging the expression for  $e_{CS}^{n+1}$  in (25) and dividing by  $(1 + 2m^2\Delta t/\epsilon^2)$ , we have

$$\begin{aligned} \|e_{CS}^{n+1}\| &= \left\| \Delta t_e \left( -\frac{m}{\epsilon^2} ((\phi^n)^{4m-1} - (\phi^n)^{2m-1}) + \Delta\phi^{n+1} \right) \right\| \\ &\leq \left\| \Delta t \left( -\frac{m}{\epsilon^2} ((\phi^n)^{4m-1} - (\phi^n)^{2m-1}) + \Delta\phi^{n+1} \right) \right\| = \|e_{SI}^{n+1}\|. \end{aligned} \quad (27)$$

Thus, the linear CS scheme is of first-order indeed when  $\Delta t \leq \Delta t_e^\infty$ .

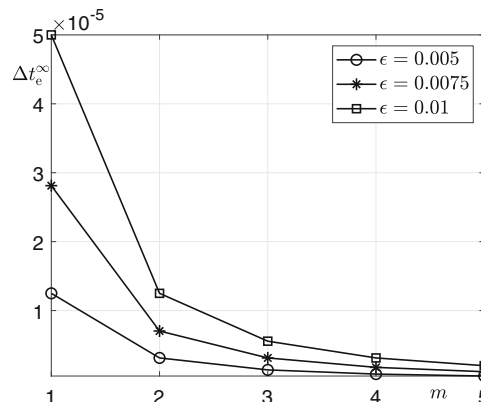


FIGURE 2 Upper bound of  $\Delta t_e$  for each order  $m$  with some different values of  $\epsilon$ .

## 2.3 | Numerical solution

To define the numerical solution, we discretize a two-dimensional domain  $\Omega = [l_x, r_x] \times [l_y, r_y]$ . Let  $L_x = r_x - l_x$ ,  $L_y = r_y - l_y$  be the lengths of  $x$ - and  $y$ -directions, respectively, and  $N_x, N_y$  be positive even integers. Consequently, we can define  $h_x = L_x/N_x$  and  $h_y = L_y/N_y$  as the space step sizes for  $x$ - and  $y$ -directions, respectively. Furthermore, the discrete points are denoted as  $(x_i, y_j) = (l_x + (i - 0.5)h_x, l_y + (j - 0.5)h_y)$  where  $1 \leq i \leq N_x$  and  $1 \leq j \leq N_y$  are integers. Let  $\phi_{ij}^n$  be an approximation of  $\phi(x_i, y_j, t_n)$ , where  $t_n = n\Delta t$  and  $\Delta t$  is the time step size. For the given discrete approximations  $\{\phi_{ij}^n | i = 1, \dots, N_x \text{ and } j = 1, \dots, N_y\}$ , their discrete cosine transforms are defined as follows:

$$\hat{\phi}_{pq}^n = \alpha_p \beta_q \sum_{i=1}^{N_x} \sum_{j=1}^{N_y} \phi_{ij}^n \cos(\xi_p \pi x_i) \cos(\eta_q \pi y_j),$$

$$p = 1, \dots, N_x \text{ and } q = 1, \dots, N_y,$$

where  $\xi_p = (p - 1)/(R_x - L_x)$ ,  $\eta_q = (q - 1)/(R_y - L_y)$ ,

$$\alpha_p = \begin{cases} \sqrt{1/N_x}, & p = 1 \\ \sqrt{2/N_x}, & 2 \leq p \leq N_x \end{cases}, \text{ and } \beta_q = \begin{cases} \sqrt{1/N_y}, & q = 1 \\ \sqrt{2/N_y}, & 2 \leq q \leq N_y \end{cases}.$$

Consequently, the inverse discrete Fourier transform is defined as follows:

$$\phi_{ij}^n = \sum_{p=1}^{N_x} \sum_{q=1}^{N_y} \alpha_p \beta_q \hat{\phi}_{pq}^n \cos(\xi_p \pi x_i) \cos(\eta_q \pi y_j).$$

Let us assume that

$$\phi(x, y, n\Delta t) = \sum_{p=1}^{N_x} \sum_{q=1}^{N_y} \alpha_p \beta_q \hat{\phi}_{pq}^n \cos(\xi_p \pi x) \cos(\eta_q \pi y).$$

We can represent the Laplacian as the linear combination of coefficients in the Fourier space as follows:

$$\Delta \phi(x, y, n\Delta t) = - \sum_{p=1}^{N_x} \sum_{q=1}^{N_y} \left[ (\xi_p \pi)^2 + (\eta_q \pi)^2 \right] \alpha_p \beta_q \hat{\phi}_{pq}^n \cos(\xi_p \pi x) \cos(\eta_q \pi y).$$

Therefore, we deduce the following numerical solution from Equation (23),

$$\hat{\phi}_{pq}^{n+1} = \frac{\hat{\phi}_{pq}^n - \Delta t \epsilon \hat{f}_m(\phi_{ij}^n)/\epsilon^2}{1 + \pi^2 \Delta t \epsilon (\xi_p^2 + \eta_q^2)},$$

where  $f_m(\phi) = F'_m(\phi)$ . For the remainder of this article, we use only a uniform spatial step, that is,  $h = h_x = h_y$  for simplicity. Although we present the numerical solution only in two-dimensional space, it can be extended to one- and three-dimensional spaces in a similar manner.

## 3 | NUMERICAL RESULTS

In this section, numerical simulation results are provided in order to verify the effect of time step modification with respect to the order  $m$  of the free energy function.

### 3.1 | Adjusting $\epsilon$ for each order $m$

First, an appropriate value of the interfacial parameter  $\epsilon$  with respect to exponent  $m$  of the polynomial potential  $F_m(\phi)$  should be derived. The hAC equation has a different transition width for each order  $m$  because the length of the interval



at which the value of  $F'_m(\phi)$  is very close to 0 increases as the order  $m$  increases (see Figure 3). In other words, we adjust the value of  $\epsilon$  to appropriately compensate for the reduced transition width.

We denote the transition width as  $\zeta$ , which is approximated as the length between points  $x_a$  and  $x_b$  satisfying  $\phi(x_a) \approx -0.95$  and  $\phi(x_b) \approx 0.95$ , respectively, in a numerical equilibrium state (see Figure 4A). The numerical equilibrium is defined when the difference between two consecutive solutions is less than  $10^{-8}$ , that is,  $\|\phi^{n+1} - \phi^n\|_2 < 10^{-8}$  where  $\|\cdot\|_2$  is the discrete  $l_2$ -norm. We use a sufficiently small time step,  $\Delta t \approx \Delta t_\epsilon$ . Table 1 lists the thickness of the transition layer  $\zeta$  with several  $\epsilon$  and  $m$ . Subsequently, we generate a linear function using the least-squares method (see Figure 4B) using the data in Table 1 to approximate the suitable value of  $\epsilon$  with respect to the order  $m$ .<sup>18</sup> The following are the best fitted lines obtained using the least-squares method:

$$\begin{aligned} \epsilon_1(\zeta) &= 0.1748\zeta + 0.0029, \\ \epsilon_2(\zeta) &= 0.2741\zeta - 0.0004, \\ \epsilon_3(\zeta) &= 0.3118\zeta - 0.0004, \\ \epsilon_4(\zeta) &= 0.3338\zeta - 0.0009, \\ \epsilon_5(\zeta) &= 0.3429\zeta - 0.0002. \end{aligned}$$

Note that  $\epsilon_m(\zeta)$  is the approximate value of  $\epsilon$  for each exponent  $m$  with a moderate transition length  $\zeta$ .

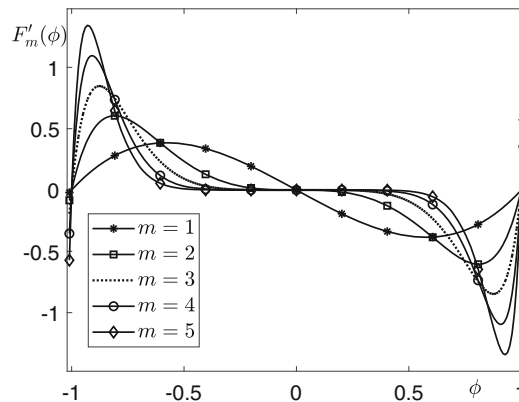


FIGURE 3 Graph of  $F'_m(\phi)$  in  $[-1, 1]$

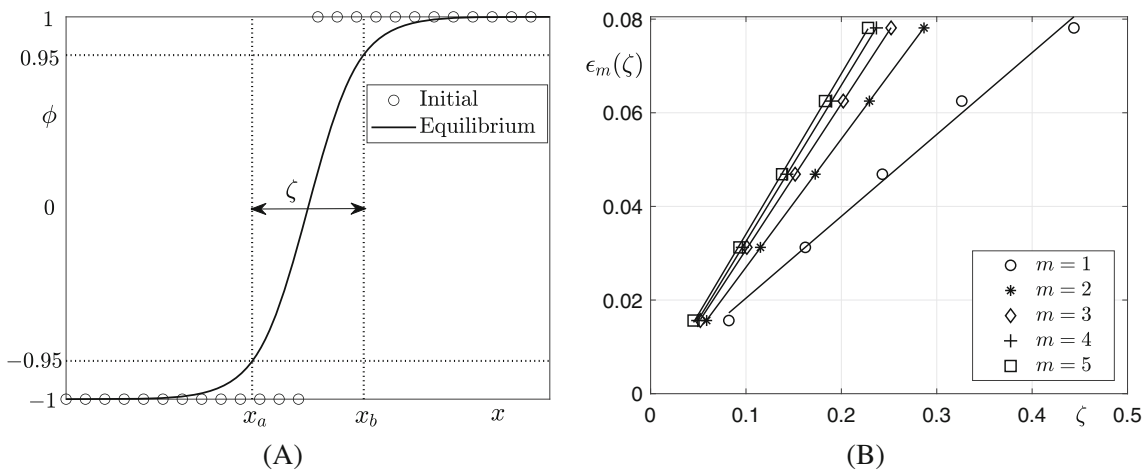


FIGURE 4 (A) Schematic of interface transition layer. (B) Data fitted linear functions to approximate suitable value of  $\epsilon$  with respect to the exponent  $m$ .



Now that we have obtained the adjusted value of  $\epsilon_m$  for each order, we provide  $\Delta t$  versus  $\Delta t_e$  plot with the upper bound  $\Delta t_e^\infty$  (dotted lines) for each order  $m$  in Figure 5. For each marker from left to right, each time step (horizontal axis) varies as  $\Delta t = 10^{-3}h^2, 10^{-2}h^2, 10^{-1}h^2, h^2, 10h^2$ . The red line represents the one-to-one ratio of  $\Delta t$  to  $\Delta t_e$ . The parameters are  $h = 1/128$  and  $\epsilon = \epsilon_m(8h)$ . According to Figure 5, the difference in the scale of two time steps is not significant when  $\Delta t < 10^{-2}h^2$  and  $\Delta t_e$  is close to its upper bound when  $\Delta t \approx 10h^2$  regardless of the order  $m$ . Table 2 lists the ratios of  $\Delta t$  to  $\Delta t_e$  for  $m = 1, 2, 3, 4,$  and  $5$ . The result yields the difference between two time steps become severe when  $\Delta t > 10^{-1}h^2$ , which compared to  $h^2/2d$  that is the time stability condition of explicit scheme for the diffusion equation in three-dimensional space ( $d = 3$ ).<sup>34</sup>

### 3.2 | Accuracy test

In this section, an accuracy test for the linear CS scheme with the effective time step is performed according to various exponents  $m$ .

**TABLE 1** Scaled thickness of interfacial transition layer  $\zeta/h$  with respect to some  $\epsilon$  and  $m$ .

Parameters	$\epsilon/h = 2$	$\epsilon/h = 4$	$\epsilon/h = 6$	$\epsilon/h = 8$	$\epsilon/h = 10$
$m = 1$	10.5002	20.7622	31.1006	41.7560	56.8054
$m = 2$	7.5219	14.7375	22.0905	29.3624	36.6892
$m = 3$	6.6748	12.9169	19.3987	25.8567	32.2747
$m = 4$	6.3304	12.3160	18.2838	24.2870	30.3053
$m = 5$	5.7637	11.9141	17.6404	23.3996	29.1785

Note: We use  $h = 1/128$  and truncate the values of thickness in the fourth decimal place.

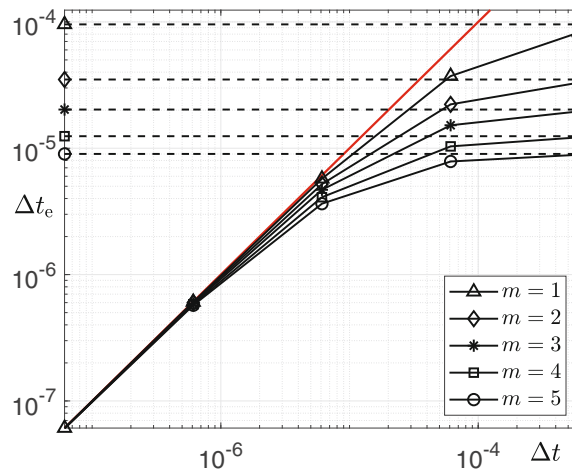


**FIGURE 5** Plot of the original time step  $\Delta t$  versus the effective time step  $\Delta t_e$ . Each dotted line with a marker is the upper bound of corresponding order and the red-colored line represents the one-to-one ratio. Note that both axes are on log-scale.

**TABLE 2** Ratios of  $\Delta t$  to  $\Delta t_e$  for  $m = 1, 2, 3, 4,$  and  $5$

Parameters	$\Delta t = 10^{-3}h^2$	$\Delta t = 10^{-2}h^2$	$\Delta t = 10^{-1}h^2$	$\Delta t = h^2$	$\Delta t = 10h^2$
$m = 1$	1.0068	1.0677	1.6770	7.7702	68.7016
$m = 2$	1.0049	1.0490	1.4901	5.9012	50.0117
$m = 3$	1.0030	1.0302	1.3015	4.0155	31.1547
$m = 4$	1.0017	1.0174	1.1744	2.7443	18.4427
$m = 5$	1.0006	1.0064	1.0639	1.6387	7.3867

Note:  $h = 1/128$ .

### 3.2.1 | Temporal accuracy

First, we measure the convergence rate in time which is expected to be of first order. Here, we use  $N_x = N_y = 128$ ,  $h = 1/128$ , and  $\epsilon = \epsilon_m(8h)$ . The following initial condition is employed:

$$\phi(x, y, 0) = 0.95 \cos\left(\frac{2\pi x}{L_x}\right) \cos\left(\frac{2\pi y}{L_y}\right).$$

Figure 6 depicts the convergence rate of the rewritten scheme (23) represented by the slope of the time step  $\Delta t_e$  versus  $l_2$ -errors  $\|\phi^{n,\Delta t_{ref}} - \phi^{n,\Delta t_e}\|_2$  where  $10^{-10} < \Delta t_{ref} = 2^{-17} \Delta t_e^\infty < 10^{-9}$  for all  $m = 1, 2, 3, 4$ , and 5. The final times are set to  $T = 11\Delta t_e^\infty$  for Figure 6A and  $T = 24\Delta t_e^\infty$  for Figure 6B, respectively. A time step  $\Delta t_e$  varies  $2^{-4} \Delta t_e^\infty, 2^{-3} \Delta t_e^\infty, \dots, \Delta t_e^\infty$  in Figure 6A and  $\Delta t_e^\infty, \dots, 2^3 \Delta t_e^\infty$  in Figure 6B, respectively, for each order  $m = 1, 2, 3, 4$ , and 5. Note that we directly assign a value to  $\Delta t_e$  to verify whether Equation (23) is of first-order. According to Figure 6A, Equation (23) is of first-order in time though the accuracy slightly degrades from 1 as the time step approaches the upper bound. Moreover, the stability of the numerical solution is not guaranteed for a time step that exceeds the upper bound, as expected, as depicted in Figure 6B.

In the next step, the convergence rate of Equation (10) are measured by varying the time step  $\Delta t = 2^{-13}T, 2^{-10}T, \dots, 2^{-2}T$  when the final time is  $T = 10h^2$  and  $\Delta t_{ref} = 2^{-18}T \approx 10^{-9}$ . Figure 7 shows the convergence rate of the linear CS scheme via  $l_2$ -errors  $\|\phi^{n,\Delta t_{ref}} - \phi^{n,\Delta t}\|_2$  versus the time step  $\Delta t$  plot and the upper bound of the effective time step. Note that we employ the same parameters and initial condition as those listed above. As depicted in Figure 7, there are considerable effects to the accuracy of scheme when  $\Delta t$  exceeds  $\Delta t_e^\infty$ , regardless of order  $m$ . This provides a rationale for using the effective time step.

### 3.2.2 | Spatial accuracy

We now examine the accuracy in space with respect to  $m = 1, 2, 3, 4$ , and 5. For the reference solution, we employ  $N_{x_{ref}} = N_{y_{ref}} = 512$ ,  $h_{ref} = 1/512$ , and  $\epsilon = \epsilon_m(16h_{ref})$ . Note that we fix the time step size to be sufficiently small as  $\Delta t = 10^{-7}$  such that  $\Delta t_e \approx \Delta t$  for  $1 \leq m \leq 5$  and set up the final time as  $T = 10^{-6}$ . Figure 8 shows the exponential convergence rate in space for both schemes for hAC equations with varying orders. Here, we use the following initial condition:

$$\phi(x, y, 0) = \tanh\left(\frac{0.2 - \sqrt{x^2 + y^2}}{\sqrt{2}\epsilon_0}\right),$$

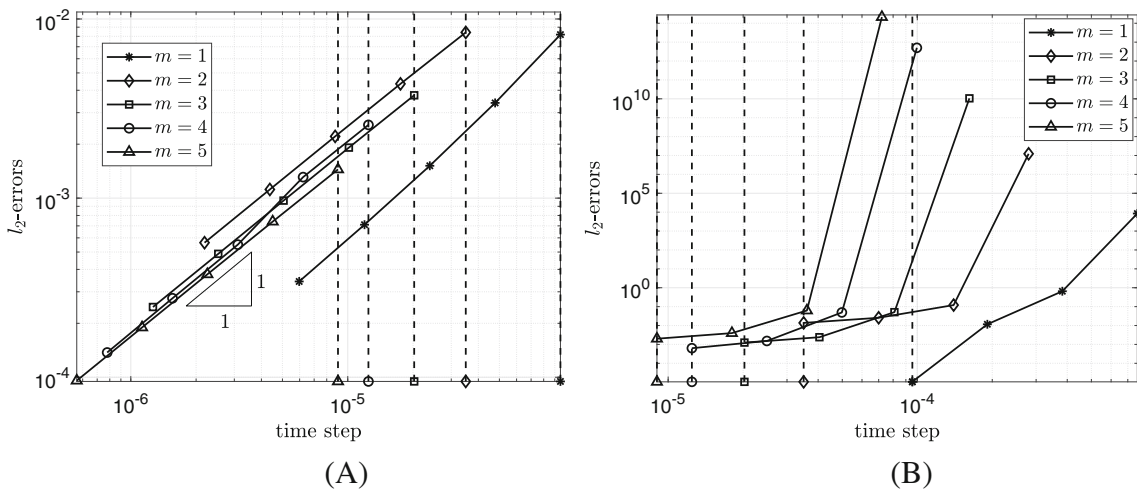
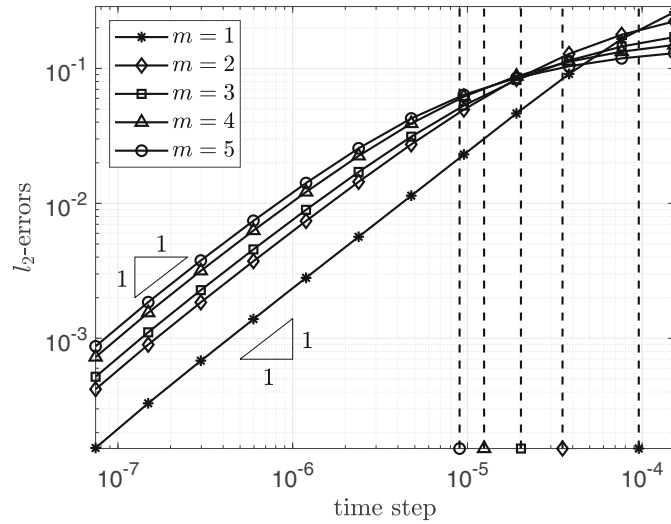
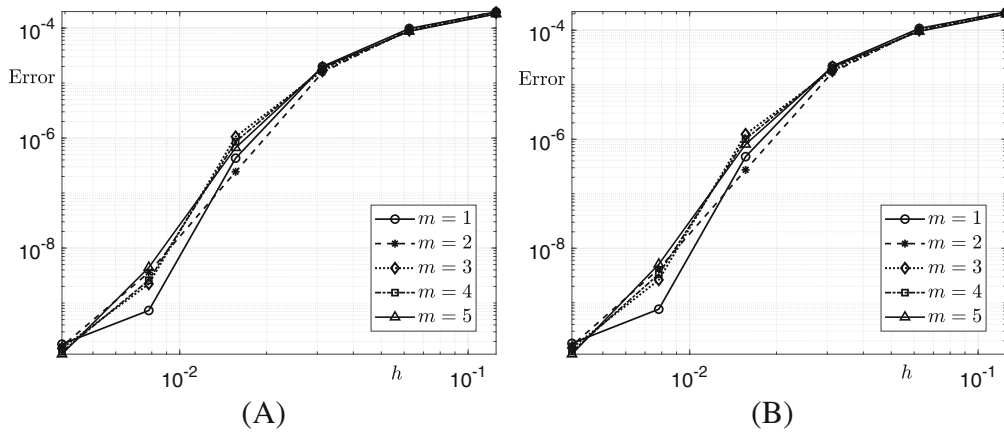


FIGURE 6 Time step  $\Delta t_e$  versus  $l_2$ -errors  $\|\phi^{n,\Delta t_{ref}} - \phi^{n,\Delta t_e}\|_2$ . Each dotted-line with marker is the upper bound. Note that both axes are on log-scale. (A)  $\Delta t_e \leq \Delta t_e^\infty$ ; (B)  $\Delta t_e \geq \Delta t_e^\infty$



**FIGURE 7** Time step  $\Delta t$  versus  $l_2$ -errors  $\|\phi^{n,\Delta t_{ref}} - \phi^{n,\Delta t}\|_2$ . Each dotted-line with marker is the upper bound of corresponding order. Note that both axes are on log-scale.



**FIGURE 8** Illustration of exponential convergence rate in space to (A) linear CS scheme using  $\Delta t$  and (B) semi-implicit scheme using  $\Delta t_e$  with varying the orders  $m = 1, 2, 3, 4,$  and  $5$ . Note that both axes are on log-scale.

where  $\epsilon_0 = 0.02$ . Note that an error is defined as follows:

$$\text{Error} = \|\phi_{h_{ref}}^n - \phi_h^n\|_2.$$

We confirm the spatial accuracy in space indeed in both cases, and the errors are nearly similar because there is a slight difference between the time step scales  $\Delta t$  and  $\Delta t_e$ .

### 3.3 | Numerical energy stability

In this section, we demonstrate the energy stability of Equation (23) by computing numerically Equation (7). First, we discretize Equation (7) in both time and space as follows:

$$\begin{aligned} \mathcal{E}^h(\phi^n) = & \sum_{i=1}^{N_x} \sum_{j=1}^{N_y} \frac{1}{4\epsilon^2} \left[ (\phi_{ij}^n)^{2m} - 1 \right]^2 h^2 \\ & + \frac{1}{2} \sum_{i=1}^{N_x-1} \sum_{j=1}^{N_y-1} \left[ (\phi_{i+1,j}^n - \phi_{ij}^n)^2 + (\phi_{i,j+1}^n - \phi_{ij}^n)^2 \right]. \end{aligned} \tag{28}$$

Since we prove the non-increasing discrete energy property in Equation (11) and this fact is also valid for Equation (23), we depict the energy dissipation in Figure 9 as numerically for  $m = 1, 2, 3, 4,$  and  $5$ . Here, we adopt the following initial condition:

$$\phi(x, y, 0) = 0.5\text{rand}(-1, 1),$$

where  $\text{rand}(a, b)$  denotes a random number between  $a$  and  $b$ . The parameters used are  $N_x = N_y = 128, h = 1/128,$  and  $\epsilon = \epsilon_m(8h)$ . We take two time step scales:  $\Delta t_1 = 10^{-6}$  and  $\Delta t_2 = 10^{-4}$ . Figure 9 shows the discrete energy (28) dissipation using  $\Delta t_1$  and  $\Delta t_2,$  their effective time steps, and the upper bound  $\Delta t_e^\infty$  for each order  $m$ . As shown in Figure 9, the numerical energy stability is verified indeed. In particular, when the time step scale is small ( $\Delta t_1$ ), the energy dissipations of the two schemes are almost the same, but when the time step scale is large ( $\Delta t_2$ ), the results are different. For the second case, the result obtained using the effective time step converges to that obtained when  $\Delta t_e^\infty$  as depicted in the enlarged axes (blue color) of Figure 9.

### 3.4 | Maximum-principle preservation

To verify the discrete maximum-principle preservation, we perform numerical simulations by varying the order  $m$  until  $T = h$ . The parameters employed are  $N_x = N_y = 256, h = 1/256, \epsilon = \epsilon_m(8h),$  and  $\Delta t = 0.1h$  with the following initial condition:

$$\phi(x, y, 0) = 0.9 \cos\left(\frac{2\pi x}{L_x}\right) \cos\left(\frac{2\pi y}{L_y}\right).$$

Figure 10 shows that the results agree well with theory.

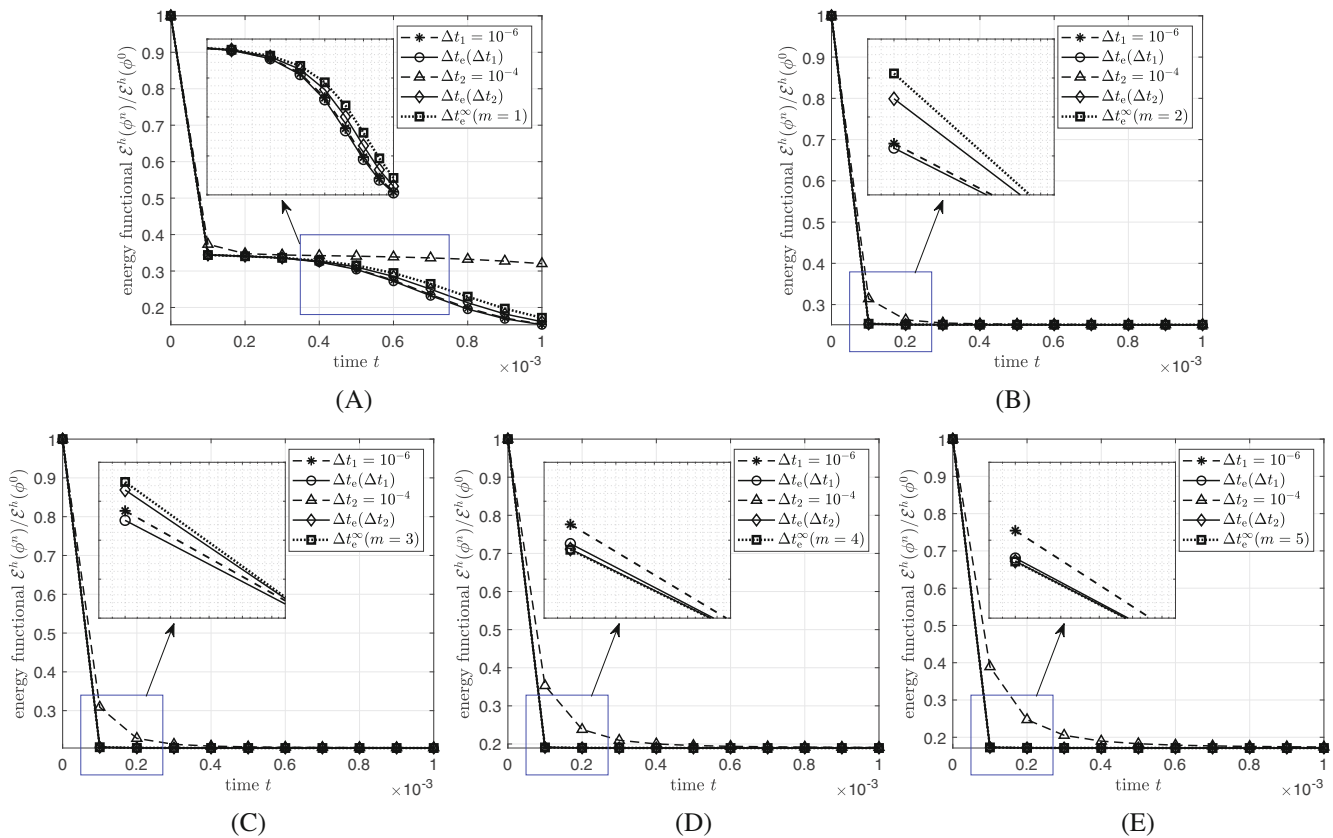


FIGURE 9 Discrete energy (28) dissipation over time with the varying orders  $m = 1, 2, 3, 4,$  and  $5$ . Note that the boxed region (blue color) is shown enlarged with the horizontal axis on log-scale. (A)  $m = 1$ ; (B)  $m = 2$ ; (C)  $m = 3$ ; (D)  $m = 4$ ; (E)  $m = 5$

### 3.5 | Motion by mean curvature

In this section, we confirm that the motion by mean curvature property is satisfied in the hAC equation and further verify the effect of  $\Delta t_e$  through the errors between the analytical and numerical solutions in the comparison test. Let us consider the minimum distance between the elements of two sets  $A$  and  $B$  as  $\text{dist}(A, B)$  and define the local coordinates as  $r(\mathbf{x}, t) = \text{dist}(\mathbf{x}, \Gamma(t)) \text{sgn}(\phi(\mathbf{x}, t))$  where  $\Gamma(t) = \{\mathbf{x} \mid \phi(\mathbf{x}, t) = 0\}$  is a zero-level set over time, and  $\text{sgn}(\cdot)$  is a sign function. We define  $\mathbf{n} = -\nabla\phi/|\nabla\phi|$  is the outward unit normal vector of the interface. Figure 11 shows the local coordinate system  $r(\mathbf{x}, t)$ . Although the high-order potential  $F_m(\phi)$  is not strictly bistable for  $m > 1$  because  $F_m''(0) = 0$ , the condition can be weakened to hold locally near  $\pm 1$  which is the minimum value of  $F_m(\phi)$ .<sup>13</sup> Thus, the following relation is formally proven:

$$\phi_t = -\frac{F_m'(\phi)}{\epsilon^2} + \phi_{rr} + \kappa\phi_r,$$

and  $-F_m'(\phi)/\epsilon^2 + \phi_{rr} \approx 0$  as  $\epsilon \rightarrow 0$ ; hence, the zero-level set  $\Gamma(t)$  approaches a surface that follows the corresponding geometric law  $V = -\kappa$ , where  $V$  is the normal velocity of the surface and  $\kappa$  is the mean curvature.<sup>13,35,36</sup>

Let  $R_0$  and  $R(t)$  be the initial radius and the radius at time  $t$  of the  $d$ -dimensional sphere, respectively. The geometric law has the following form:

$$V = \frac{dR(t)}{dt} = -\frac{d}{R(t)},$$

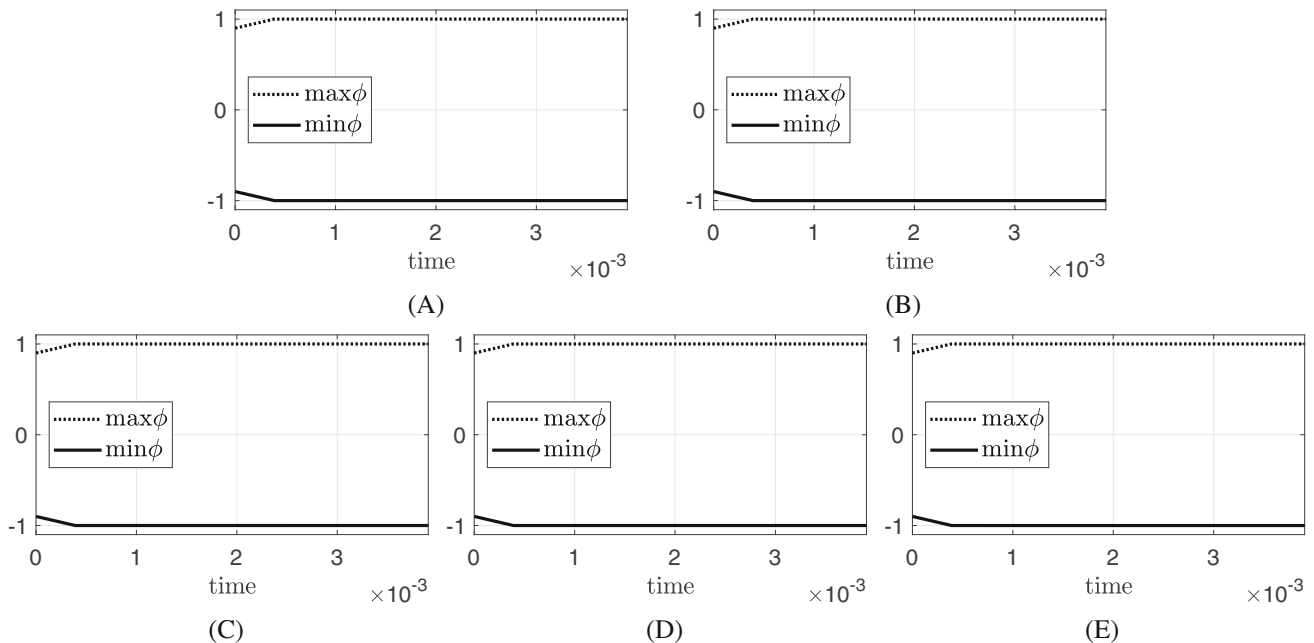


FIGURE 10 Maximum and minimum values of  $\phi$  versus time with different  $m$ . (A)  $m = 1$ ; (B)  $m = 2$ ; (C)  $m = 3$ ; (D)  $m = 4$ ; (E)  $m = 5$

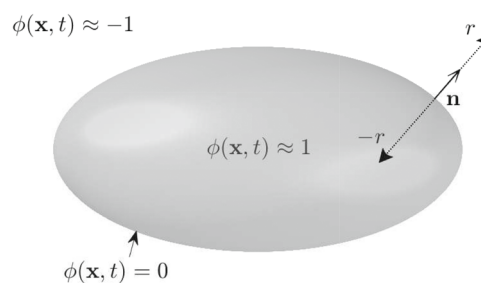


FIGURE 11 Local coordinates system  $r(\mathbf{x}, t)$  with the zero-level set  $\Gamma(t)$ .

and its solution is given as follows:

$$R(t) = \sqrt{R_0^2 - 2dt}. \quad (29)$$

For the two-dimensional case, the initial condition is as follows:

$$\phi(x, y, 0) = \tanh \frac{R_0 - \sqrt{x^2 + y^2}}{\sqrt{2\epsilon}},$$

in  $[-0.5, 0.5] \times [-0.5, 0.5]$ . The parameters employed are  $N_x = N_y = 128$ ,  $h = 1/128$ ,  $\Delta t = 0.15h^2 \approx 9.16 \times 10^{-6}$ , and  $\epsilon = \epsilon_m(10h)$ . We take  $R_0 = 0.2$  and perform the test until  $R(t) = 0$ . Figure 12 shows snapshots of the shrinking circles with exponents  $m = 1$  (first row) and 5 (second row). Since we regard  $\phi = 0$  as the interface, the circles disappear at the final time in both cases, as shown in Figure 12C. To confirm the effect of  $\Delta t_e$  more precisely, we compare the radii obtained under the same parameters, except for the time step using (10) and (23) for the analytic solution simultaneously until  $R(t) \approx 0$ . Figure 13 depicts  $R(t)$  over time obtained using Equations (10), (23), and (29) with the varying exponents  $m = 1, 2, 3, 4$ , and 5. The parameters are employed as in the previous test, but for  $T = 0.015$ . Note that the number of iterations performed for the same final time  $T$  is different for both schemes. That is, a difference in the time evolution occurs. Therefore, the same final time is applied to both schemes; the time rescaling effect becomes more severe as the time step size  $\Delta t_e$  employed in (23) approaches  $\Delta t_e^\infty$ , that is, when  $\Delta t$  increases. As shown in Figure 13, it is confirmed that the solution obtained by using the effective time step is more accurate for each exponent  $m$  indeed. Moreover, the effect of  $\Delta t_e$  increases as  $m$  increases. An important fact at this point is that  $\Delta t \approx \Delta t_e^\infty$  yields the time rescaling problem even though  $\Delta t_e$  is not close to  $\Delta t_e^\infty$ , that is, when  $\Delta t$  is not extremely large.

We further extend the solution (29) to three-dimensional case. The initial condition is as follows:

$$\phi(x, y, z, 0) = \tanh \frac{R_0 - \sqrt{x^2 + y^2 + z^2}}{\sqrt{2\epsilon}},$$

in  $[-0.5, 0.5] \times [-0.5, 0.5] \times [-0.5, 0.5]$ . Here, the parameters are employed as  $N_x = N_y = N_z = 100$ ,  $h = 1/100$ ,  $\Delta t = 0.15h^2 = 1.5 \times 10^{-5}$ ,  $\epsilon = \epsilon_m(8h)$ ,  $R_0 = 0.2$ , and the test is performed until  $R(t) = 0$ . Figure 14 illustrates snapshots of shrinking spheres with orders  $m = 1$  (first row) and 5 (second row). The spheres vanished, as depicted in Figure 14C, similar to the two-dimensional case. We proceed with the same test to examine the impact of the effective time step in three-dimensional space. Figure 15 describes  $R(t)$  over time obtained using Equations (10), (23), and (29) with the varying orders  $m = 1, 2, 3, 4$ , and 5. The parameters are the same as in the previous test but for  $T = 0.0075$ .

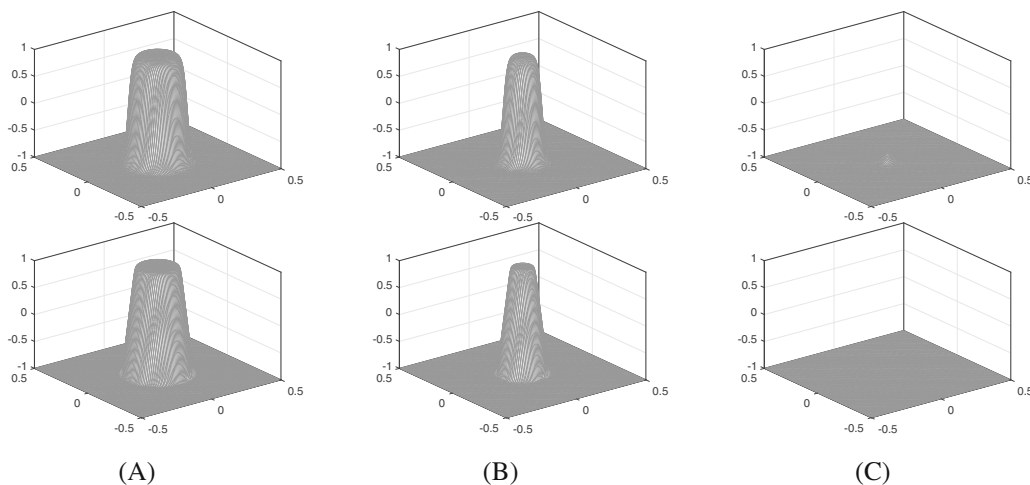


**FIGURE 12** Snapshots of shrinking circles governed by the mean curvature flow at (A)  $t = 0.006$ , (B)  $t = 0.014$ , and (C)  $t = 0.02$ . The first row is  $m = 1$  case and the second row is  $m = 5$  case.

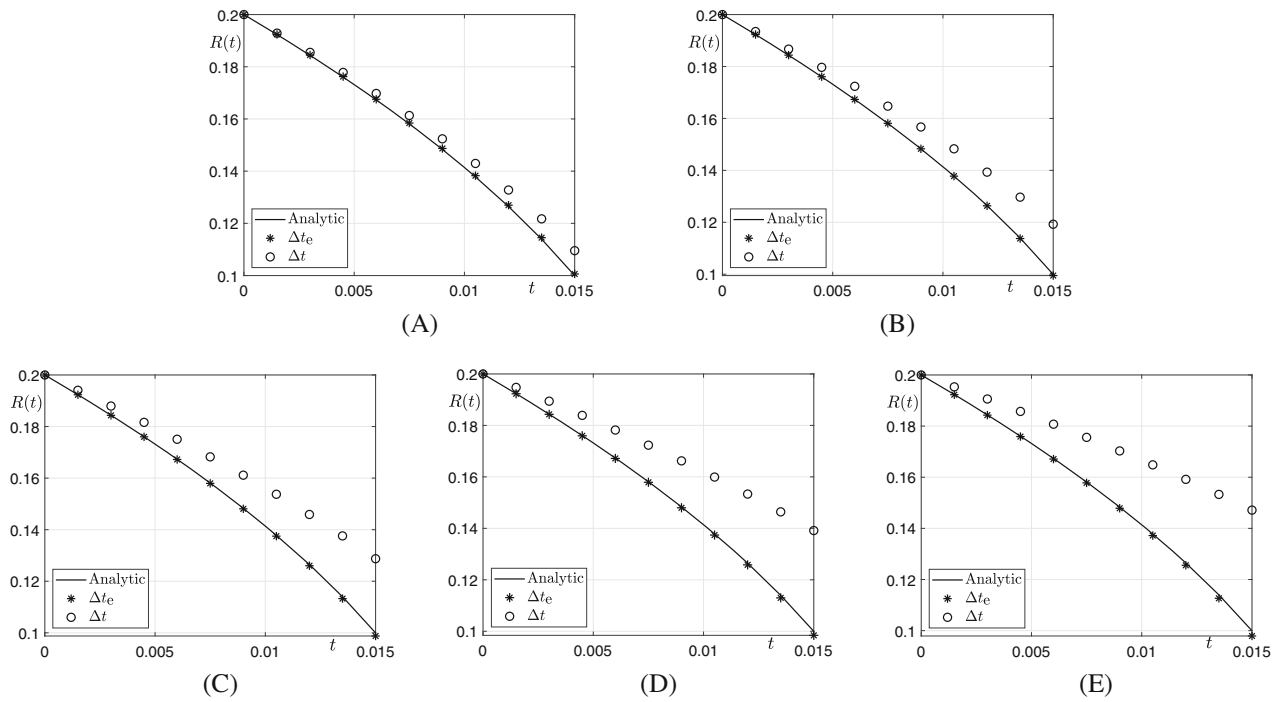


**FIGURE 13** Comparison plot of  $R(t)$  obtained by three different ways: analytic, linear CS method using  $\Delta t$ , and semi-implicit scheme using  $\Delta t_e$  in two-dimensional space. The parameters are adopted as same as used in Figure 12. Note that the value of  $\Delta t_e$  is approximated as (A)  $0.9374\Delta t$ , (B)  $0.8577\Delta t$ , (C)  $0.7770\Delta t$ , (D)  $0.6839\Delta t$ , and (E)  $0.6070\Delta t$ , respectively. (A)  $m = 1(\Delta t_e^\infty \approx 1.37 \times 10^{-4})$ ; (B)  $m = 2(\Delta t_e^\infty \approx 5.52 \times 10^{-5})$ ; (C)  $m = 3(\Delta t_e^\infty \approx 3.19 \times 10^{-5})$ ; (D)  $m = 4(\Delta t_e^\infty \approx 1.98 \times 10^{-5})$ ; (E)  $m = 5(\Delta t_e^\infty \approx 1.41 \times 10^{-5})$

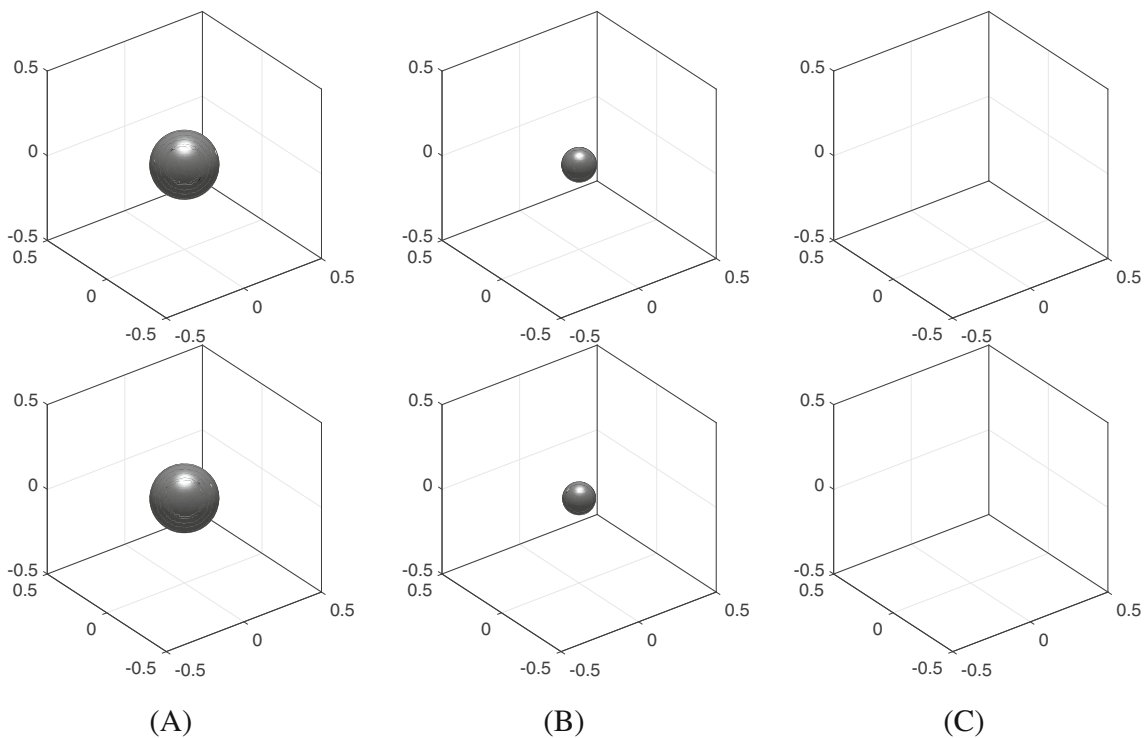


**FIGURE 14** Snapshots of shrinking spheres governed by the mean curvature flow at (A)  $t = 0.002$ , (B)  $t = 0.008$ , and (C)  $t = 0.01$ . The first row is  $m = 1$  case and the second row is  $m = 5$  case.



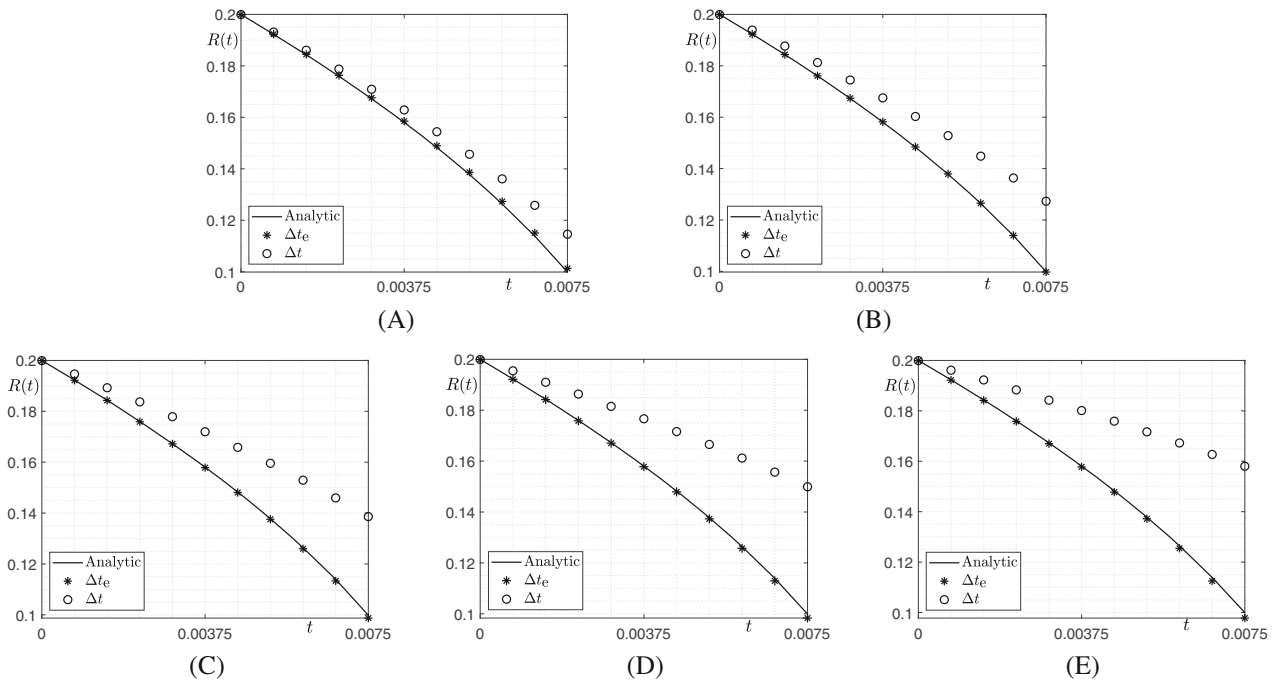


**FIGURE 15** Comparison plot of  $R(t)$  obtained by three different ways: analytic, linear CS method using  $\Delta t$ , and semi-implicit scheme using  $\Delta t_e$  in three-dimensional space. The parameters are employed as same as used in Figure 14. Note that the value of  $\Delta t_e$  is approximated as (A)  $0.9048\Delta t$ , (B)  $0.7943\Delta t$ , (C)  $0.6905\Delta t$ , (D)  $0.5811\Delta t$ , and (E)  $0.4972\Delta t$ , respectively. (A)  $m = 1(\Delta t_e^\infty \approx 1.43 \times 10^{-4})$ ; (B)  $m = 2(\Delta t_e^\infty \approx 5.79 \times 10^{-5})$ ; (C)  $m = 3(\Delta t_e^\infty \approx 3.35 \times 10^{-5})$ ; (D)  $m = 4(\Delta t_e^\infty \approx 2.08 \times 10^{-5})$ ; (E)  $m = 5(\Delta t_e^\infty \approx 1.48 \times 10^{-5})$

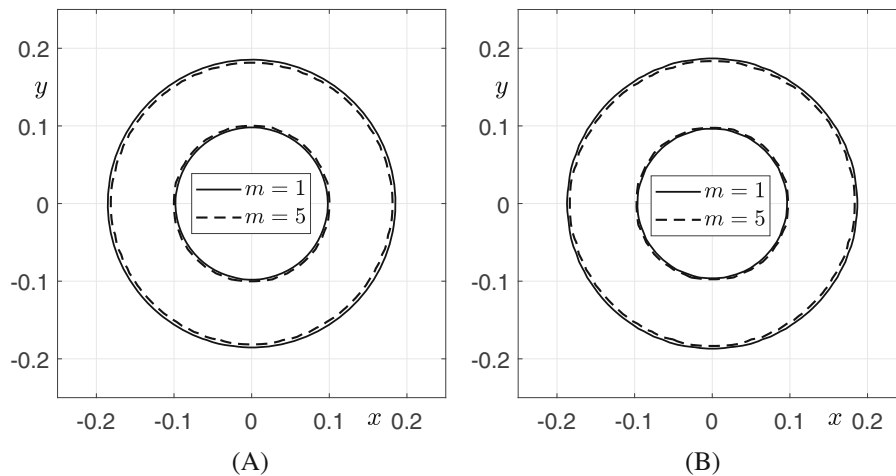


**FIGURE 16** Transition width comparison between the two numerical solutions ( $m = 1$  and  $5$ ) at the same  $R(t) \approx 0.1414$ . (A) Two-dimensional case ( $t = 0.01$ ). (B) Three-dimensional case ( $t = 0.005$ )

Similar to the results in two-dimensional space, the effect of the time step modification is conspicuous in the three-dimensional case, as shown in Figure 15. Overall, it is confirmed that the motion by mean curvature property remains independent of the exponent  $m$ , as shown in Figures 12 and 14, although the shape of the transition layer is slightly different depending on the order. A comparison of the transition widths between the two numerical solutions ( $m = 1$  and  $5$ ) at the same  $R(t) \approx 0.1414$  is presented in Figure 16. It is verified that the speed and transition width of the mean curvature flow do not differ significantly depending on the dimension of the domain and order  $m$  when the effective time step is employed. More precisely, there is a slight difference between the two numerical solutions because the values of  $\alpha$  and  $\epsilon$  affect the effective time step  $\Delta t_e$  and the initial conditions. However, this fact does not affect the conclusions.

## 4 | CONCLUSIONS

An effective time step analysis of the CS scheme for the hAC equation is presented herein. It was verified that the time step rescaling problem of the CS scheme and the distinct slow dynamics of the hAC equation depending on the orders were reported in several studies.<sup>19,31,32</sup> Owing to the high nonlinearity of the hAC equation, we adopted the linear CS scheme and reformulated it to a semi-implicit scheme using a different time step scale to investigate the effect of time step scaling. We theoretically proved that the linear CS scheme satisfies the two intrinsic properties of the hAC equation, energy stability, and maximum-principle preservation, and confirmed that it is valid in the reformulated scheme. These properties are also shown numerically. The convergence rate was of first-order in time only when the time step was within the upper bound. To check how accurately solved by the semi-implicit scheme using  $\Delta t_e$  rather than the linear CS scheme using  $\Delta t$  for the delayed dynamics according to the increase in order, the motion by mean curvature was used. We confirmed that the effect of  $\Delta t_e$  was prominent, and the numerical results agreed well with the theoretical results. In future work, we will apply this analysis to multiphase flow modeling and simulation because the temporal evolution can be approximated fairly accurately via the effective time step.

## ACKNOWLEDGMENTS

The first author (Seunggyu Lee) was supported by a Korea University Grant and the National Research Foundation of Korea (NRF) Grant funded by the Korea government (MSIP) (No. 2020R1A2C1A01100114). The author (Sungha Yoon) was supported by the National Research Foundation of Korea (NRF) Grant funded by the Ministry of Science and ICT of Korea (MSIT) (No. 2019R1A6A1A11051177). The author (Hyundong Kim) was supported by the Basic Science Research Program through the National Research Foundation of Korea (NRF) funded by the Ministry of Education, Republic of Korea (NRF-2020R1A6A3A13077105). The corresponding author (Junseok Kim) was supported by a Grant from the Korea University Grant. The authors are grateful to the reviewers for their contributions to improving this article.

## CONFLICT OF INTEREST

The authors declare no potential conflicts of interest.

## DATA AVAILABILITY STATEMENT

The data that support the findings of this study are available from the corresponding author upon reasonable request.

## ORCID

Junseok Kim  <https://orcid.org/0000-0002-0484-9189>

## REFERENCES

1. Allen SM, Cahn JW. A microscopic theory for antiphase boundary motion and its application to antiphase domain coarsening. *Acta Metall.* 1979;27(6):1085-1095.
2. Achleitner F, Kuehn C, Melenk JM, Rieder A. Metastable speeds in the fractional Allen–Cahn equation. *Appl Math Comput.* 2021;408:126329.
3. Budd J, van Gennip Y, Latz J. Classification and image processing with a semi-discrete scheme for fidelity forced Allen–Cahn on graphs. *GAMM-Mitteilungen.* 2021;44(1):e202100004.
4. Wang J, Li Y, Choi Y, Lee C, Kim J. Fast and accurate smoothing method using a modified Allen–Cahn equation. *Comput Aided Des.* 2020;120:102804.
5. Hu X, Li Y, Ji H. A nodal finite element approximation of a phase field model for shape and topology optimization. *Appl Math Comput.* 2018;339:675-684.
6. Yu Q, Wang K, Xia B, Li Y. First and second order unconditionally energy stable schemes for topology optimization based on phase field method. *Appl Math Comput.* 2021;405:126267.
7. Ma L, Chen R, Yang X, Zhang H. Numerical approximations for Allen–Cahn type phase field model of two-phase incompressible fluids with moving contact lines. *Commun Comput Phys.* 2017;21(3):867-889.
8. Aihara S, Takaki T, Takada N. Multi-phase-field modeling using a conservative Allen–Cahn equation for multiphase flow. *Comput Fluids.* 2019;178:141-151.
9. Yang X. A novel fully decoupled scheme with second-order time accuracy and unconditional energy stability for the Navier–Stokes equations coupled with mass-conserved Allen–Cahn phase-field model of two-phase incompressible flow. *Int J Numer Methods Eng.* 2021;122(5):1283-1306.
10. Yu Z, Wang X, Liang H, Li Z, Li L, Yue Z. Thickness debit effect in Ni-based single crystal superalloys at different stress levels. *Int J Mech Sci.* 2020;170:105357.

11. Zhao J, Wang Q, Yang X. Numerical approximations for a phase field dendritic crystal growth model based on the invariant energy quadratization approach. *Int J Numer Methods Eng*. 2017;110(3):279-300.
12. Zhang J, Chen C, Yang X. A novel decoupled and stable scheme for an anisotropic phase-field dendritic crystal growth model. *Appl Math Lett*. 2019;95:122-129.
13. Ilmanen T. Convergence of the Allen–Cahn equation to Brakke’s motion by mean curvature. *J Differ Geom*. 1993;38(2):417-461.
14. Laux T, Simon TM. Convergence of the Allen–Cahn equation to multiphase mean curvature flow. *Commun Pure Appl Math*. 2018;71(8):1597-1647.
15. Muramatsu M, Yashiro K, Kawada T, Terada K. Simulation of ferroelastic phase formation using phase-field model. *Int J Mech Sci*. 2018;146:462-474.
16. Barros de Moraes EA, Zayernouri M, Meerschaert MM. An integrated sensitivity-uncertainty quantification framework for stochastic phase-field modeling of material damage. *Int J Numer Methods Eng*. 2021;122(5):1352-1377.
17. Tsou NT, Huber J, Shu Y. A sharp interface model of compatible twin patterns in shape memory alloys. *Smart Mater Struct*. 2012;21(9):094010.
18. Shin J, Yang J, Lee C, Kim J. The Navier–Stokes–Cahn–Hilliard model with a high-order polynomial free energy. *Acta Mech*. 2020;231(6):2425-2437.
19. Lee C, Kim H, Yoon S, et al. An unconditionally stable scheme for the Allen–Cahn equation with high-order polynomial free energy. *Commun Nonlinear Sci Numer Simul*. 2021;95:105658.
20. Evans LC, Soner HM, Souganidis PE. Phase transitions and generalized motion by mean curvature. *Commun Pure Appl Math*. 1992;45(9):1097-1123.
21. Feng J, Zhou Y, Hou T. A maximum-principle preserving and unconditionally energy-stable linear second-order finite difference scheme for Allen–Cahn equations. *Appl Math Lett*. 2021;118:107179.
22. Zhang H, Yan J, Qian X, Song S. Numerical analysis and applications of explicit high order maximum principle preserving integrating factor Runge–Kutta schemes for Allen–Cahn equation. *Appl Numer Math*. 2021;161:372-390.
23. Wang X, Kou J, Gao H. Linear energy stable and maximum principle preserving semi-implicit scheme for Allen–Cahn equation with double well potential. *Commun Nonlinear Sci Numer Simul*. 2021;98:105766.
24. Li H, Song Z. A reduced-order energy-stability-preserving finite difference iterative scheme based on POD for the Allen–Cahn equation. *J Math Anal Appl*. 2020;491(1):124245.
25. Li H, Song Z, Hu J. Numerical analysis of a second-order IPDGFE method for the Allen–Cahn equation and the curvature-driven geometric flow. *Comput Math Appl*. 2021;86:49-62.
26. Montanelli H, Bootland N. Solving periodic semilinear stiff PDEs in 1D, 2D and 3D with exponential integrators. *Math Comput Simul*. 2020;178:307-327.
27. Wight CL, Zhao J. Solving Allen–Cahn and Cahn–Hilliard equations using the adaptive physics informed neural networks. *Commun Comput Phys*. 2021;29(3):930-954.
28. Eyre DJ. Unconditionally gradient stable time marching the Cahn–Hilliard equation. *MRS Online Proc Lib (OPL)*. 1998;529:39-46.
29. Choi JW, Lee HG, Jeong D, Kim J. An unconditionally gradient stable numerical method for solving the Allen–Cahn equation. *Phys A Stat Mech Appl*. 2009;388(9):1791-1803.
30. Xu J, Li Y, Wu S, Bousquet A. On the stability and accuracy of partially and fully implicit schemes for phase field modeling. *Comput Methods Appl Mech Eng*. 2019;345:826-853.
31. Lee S, Kim J. Effective time step analysis of a nonlinear convex splitting scheme for the Cahn–Hilliard equation. *Commun Comput Phys*. 2019;25(2):448-460.
32. Glasner K, Orizaga S. Improving the accuracy of convexity splitting methods for gradient flow equations. *J Comput Phys*. 2016;315:52-64.
33. Eyre DJ. An unconditionally stable one-step scheme for gradient systems; 1998:6.
34. Hundsdorfer WH, Verwer JG, Hundsdorfer W. *Numerical Solution of Time-Dependent Advection-Diffusion-Reaction Equations*. Vol 33. Springer; 2003.
35. Bao W. Approximation and comparison for motion by mean curvature with intersection points. *Comput Math Appl*. 2003;46(8-9):1211-1228.
36. Lee D, Kim J. Mean curvature flow by the Allen–Cahn equation. *Eur J Appl Math*. 2015;26(4):535-559.

**How to cite this article:** Lee S, Yoon S, Lee C, et al. Effective time step analysis for the Allen–Cahn equation with a high-order polynomial free energy. *Int J Numer Methods Eng*. 2022;123(19):4726-4743. doi: 10.1002/nme.7053